Solution-Phase Synthesis of $PdH_{0.706}$ Nanocubes with Enhanced Stability and Activity toward Formic Acid Oxidation

Yifeng Shi,[a,†] Roberto Schimmenti,[b,†] Shangqian Zhu,[c] Kartik Venkatraman,[d] Ruhui Chen,[e] Miaofang Chi,[d] Minhua Shao,[c] Manos Mavrikakis[b,*] and Younan Xia[a,e,f,*]

[a]*School of Chemical and Biomolecular Engineering, Georgia Institute of Technology, Atlanta, Georgia 30332, USA*

[b]*Department of Chemical and Biological Engineering, University of Wisconsin−Madison, Madison, Wisconsin 53706, USA*

[c]*Department of Chemical and Biological Engineering and Hong Kong Branch of the Southern Marine Science and Engineering Guangdong Laboratory, The Hong Kong University of Science and Technology, Clear Water Bay, Kowloon, Hong Kong, P. R. China*

[d]*Center for Nanophase Materials Sciences, Oak Ridge National Laboratory, Oak Ridge, Tennessee 37831, USA*

[e]*School of Chemistry and Biochemistry, Georgia Institute of Technology, Atlanta, Georgia 30332, USA*

[f]*The Wallace H. Coulter Department of Biomedical Engineering, Georgia Institute of Technology and Emory University, Atlanta, Georgia 30332, USA*

*Email: emavrikakis@wisc.edu, younan.xia@bme.gatech.edu

ABSTRACT: Palladium is one of the few metals capable of forming hydrides, with the catalytic properties being dependent on the elemental composition and spatial distribution of H atoms in the lattice. Herein, we report a facile method for the complete transformation of Pd nanocubes into a stable phase made of $PdH_{0.706}$ by treating them with aqueous hydrazine at a concentration as low as 9.2 mM. Using formic acid oxidation (FAO) as a model reaction, we systematically investigated the structure-catalytic property relationship of the resultant nanocubes with different degrees of hydride formation. The current density at 0.4 V was enhanced by four times when the nanocubes were completely converted from Pd to $PdH_{0.706}$. Based on a set of slab models with PdH(100) overlayers on Pd(100), we conducted density functional theory calculations to demonstrate that the degree of hybrid formation could influence both the activity and selectivity toward FAO by modulating the relative stability of formate (HCOO) and carboxyl (COOH) intermediates. This work provides a viable strategy for augmenting the performance of Pd-based catalysts toward various reactions without altering the loading of this scarce metal.

INTRODUCTION

Palladium is an efficient catalytic material toward many important reactions, including those related to selective hydrogenation[1] and C-C coupling,[2] as well as operation of catalytic converters[3] and fuel cells.[4-6] In particular, Pd has proven itself one of the best monometallic catalysts toward formic acid oxidation (FAO), a reaction essential to the operation of direct formic acid fuel cells (DFAFCs). The performance of Pd-based catalysts toward FAO has been extensively investigated through both theoretical[7-10] and experimental[11] approaches. Besides its intrinsic material properties, prior studies involving density functional theory (DFT) calculations and single-crystal electrode measurements have established that the FAO activities of Pd surfaces decrease in the order of Pd(100) > Pd(111) > Pd(110).[12] By leveraging the recent developments in colloidal synthesis of shape-controlled nanocrystals, both the specific and mass activities can be improved by switching from poorly-defined nanoparticles to nanocrystals enclosed by well-defined {100} facets.[4] Despite the significant progress along this line, the limited supply and ever-increasing price of Pd call for the development of new strategies capable of further enhancing the performance of a catalyst without changing the loading of this scarce metal. The reported strategies include decoration of the catalyst with SnO_2,[13] introduction of CeO_2 supports with specific surface structures,[14] removal of the adsorbed capping agents,[15] formation of thin overlayers or intermetallic structures,[16,17] and switching the crystal structure from pristine palladium to palladium hydride (PdH_x).[18, 19]

The strategy involving PdH_x is unique as Pd is one of the few metals that have the capability to form metal hydrides.[20] The formation of PdH_x not only plays a vital role in a set of catalytic reactions,[18, 19, 21-24] but also attracts wide attention in a number of fundamental studies.[21, 25-28] The bulk and surface properties of a Pd substrate can be tuned by adjusting the stoichiometry of H atoms in the Pd lattice (*i.e.*, the "x" in PdH_x). Most of the fundamental studies reported in the literature involved the use of H_2 gas as a source of H atoms.[21, 25, 27, 28] A number of alternative sources of H atoms have also been reported, with notable examples including dimethylformamide (DMF),[22] sodium borohydride ($NaBH_4$),[23] and formaldehyde (HCOH).[29] However, most of these studies could only achieve PdH_x with x up to 0.43. Although a few studies claimed that the $PdH_{0.43}$ phase fabricated using these alternative sources could outperform its Pd counterpart in both FAO and methanol oxidation,[19] the enhancement in terms of specific activity was rather limited (*e.g.*, 56% and 75% increase in terms of FAO specific activity at the peak position and 0.4 V, respectively). Moreover, the corresponding protocols typically required the use of an elevated

pressure, and the surface of the PdH_x generated using these methods were often contaminated by these organic compounds or chemical species derived from them.

Herein, we report a solution-phase method for the facile transformation of pre-synthesized nanocubes from Pd to $PdH_{0.706}$ by heating them in a dilute aqueous solution of N_2H_4. The degree of hydride formation could be controlled by adjusting the concentration of N_2H_4 involved in the treatment. Using FAO as a model reaction, we further examined the structure-catalytic property relationship of the Pd-$PdH_{0.706}$/C catalysts with different degrees of hydride formation. It was found that the catalytic activity toward FAO was strongly dependent on the content of hydride phase in the nanocubes, with those made of pure $PdH_{0.706}$ performing the best among the different samples. Upon complete conversion into the $PdH_{0.706}$ phase, the specific activity at 0.4 V was increased by four folds relative to the pristine Pd nanocubes. The structure-catalytic property relationship was also rationalized by DFT calculations and *in situ* attenuated total reflection infrared spectroscopy (ATR-IR) studies.

EXPERIMENTAL SECTION

Chemicals and Materials. Poly(vinyl pyrrolidone) (PVP, with an average molecular weight of 55,000), L-ascorbic acid (AA, BioXtra, 99%), formaldehyde solution (HCHO, 37% wt.% in H_2O), potassium bromide (KBr, 99.9%), perchloric acid (HClO4, 70%), formic acid (HCOOH, 95%), sulfuric acid (H_2SO_4, 99.999%), copper(II) sulfate ($CuSO_4$, anhydrous powder, 99.99%), and aqueous hydrazine solution (N_2H_4, 35 wt.%) were all obtained from Sigma-Aldrich. Sodium tetrachloropalladate(II) (Na_2PdCl_4, 36% Pd) was purchased from Acros Organics. All aqueous solutions were prepared using deionized (DI) water with a resistivity of 18.2 MΩ·cm at room temperature.

Synthesis of 15.8- and 6.7-nm Pd Nanocubes. The Pd nanocubes with average edge length of 15.8 nm (see Figure S1) were synthesized using a previously reported protocol.[30] In a typical synthesis, 8 mL of an aqueous solution containing 105 mg of PVP, 60 mg of AA, and 600 mg of KBr were mixed in a 25-mL glass vial and heated in an oil bath at 80 °C for 10 min under magnetic stirring, followed by the injection of 3 mL of aqueous Na_2PdCl_4 (19 mg mL^{-1}) in one shot. The reaction mixture was held at 80 °C for another 3 h. The Pd nanocubes were collected by centrifugation at 20,000 rpm, washed three times with water, and re-dispersed in water for further use. To synthesize 6.7-nm Pd nanocubes, a similar protocol was used, except that the 600 mg of

KBr was replaced with a mixture of 185 mg of KCl and 5 mg of KBr. The 6.7-nm nanocubes were collected by centrifugation at 55,000 rpm using an ultracentrifuge (Beckman).

Synthesis of Pd Octahedra. The Pd octahedra with an average edge length of 12.0 nm were synthesized through seed-mediated growth.[31] Typically, 8 mL of an aqueous solution containing 105 mg of PVP, 0.25 mL of the 6.7-nm Pd nanocubes (2.13 mg mL^{-1}), and 0.1 mL of the aqueous HCHO was preheated at 60 °C for 10 min, followed by the injection of 3 mL of aqueous Na_2PdCl_4 (9.6 mg mL^{-1}) in one shot. The reaction mixture was kept at 60 °C for 3 h. The Pd octahedra were collected by centrifugation, washed three times with water, and re-disposed in water.

Preparation of $Pd_{nanocube}$/C and Pd-$PdH_{0.706}$/C Catalysts. In a standard process, 200 mg of carbon black powders (Vulcan XC72) were dispersed in water and sonicated in an ice bath for 1 h, followed by the introduction of the aqueous suspension of Pd nanocubes (containing *ca.* 20 mg of Pd). The mixture was sonicated in the ice bath for another 1 h and the $Pd_{nanocube}$/C was collected by centrifugation at 12,100 rpm. The Pd loading was determined to be *ca*. 7.5 wt.% by inductively-coupled plasma mass spectrometry (ICP-MS). The catalyst was then dried in an oven held at 80 °C for 5 h.

The as-obtained $Pd_{nanocube}$/C catalyst was treated with aqueous N_2H_4 at various concentrations to obtain Pd-$PdH_{0.706}$/C with different degrees of hydride formation. In a typical process, 12 mg of the $Pd_{nanocube}$/C catalyst and 6 mL of water were added into a 25-mL glass vial and preheated at 95 °C for 10 min under magnetic stirring. Afterwards, 25 μL of aqueous N_2H_4 at a specific concentration (0.35, 1.4, 3, 4, 5, or 7 wt.%) was injected into the vial. The mixture was kept at 95 °C in the capped vial for another 3 h to obtain the Pd-$PdH_{0.706}$/C catalyst. The solid product was collected by centrifugation at 12,100 rpm and dried in an oven at 80 °C for 1 h before preparing catalyst ink. In our discussion, the catalysts are denoted by the final molar concentration of N_2H_4 in the vial, with 25 μL of 0.35, 1.4, 3, 4, 5, and 7 wt.% N_2H_4 solutions corresponding to 0.46, 1.8, 3.9, 5.2, 6.3, and 9.2 mM in the final reaction mixtures, respectively.

To obtain nanocubes made of pure $PdH_{0.706}$, 12 mg of the $Pd_{nanocube}$/C catalyst was dispersed in 6 mL of water hosted in a 25-mL vial and preheated at 95 °C for 10 min under magnetic stirring, followed by the injection of 25 μL of 7 wt% N_2H_4 solution. The vial was then capped and held at 95 °C for another 3 h, and the catalyst was collected by centrifugation and re-dispersed in 6 mL water hosted in a different 25-mL vial for the second round of treatment. The same treatment was repeated six times to obtain nanocubes made of pure $PdH_{0.706}$. It is worth pointing out that the final

composition of the Pd-$PdH_{0.706}$/C catalyst is dependent on the volume of the solution relative to the volume of the vial. Any change to the solution volume or vial volume will alter the pressure in the vial, affecting the degree of hydride formation.

Preparation of $Pd_{octahedron}$/C and Pd-$PdH_{0.706}$/C Catalysts. The protocol was similar to what was used for $Pd_{nanocube}$/C, except that the Pd loading was changed to 10 wt.%. The Pd-$PdH_{0.706}$/C and $PdH_{0.706}$/C samples shown in Figure S2 were obtained by treating Pd octahedral nanocrystals with 7 wt.% aqueous N_2H_4 once and 11 times, respectively.

Electrochemical Measurements. All electrochemical measurements were carried out in a three-electrode cell connected with CHI 600E potentiostat electrochemical workstation at room temperature. Glassy carbon (GC, 5mm in diameter) and Pt mesh (1×1 cm) served as the working and counter electrodes, respectively, for all measurements. Reversible hydrogen electrode (RHE, HydroFlex, Gasketel) served as a reference electrode in the FAO activity test. For Cu underpotential deposition (UPD), saturated calomel electrode (SCE) was used as a reference electrode. Catalyst ink was prepared by mixing 2.5 mg of the dried carbon-supported nanocrystals, 10 μL of Nafion (5 wt. %, Aldrich), and 2.5 mL of ethanol (99.5%, VWR) in a glass vial and sonicated in an ice bath for 1 h. Prior to all electrochemical measurements, the GC electrode was polished with 0.3-μm and then 0.05-μm Al_2O_3 powders, followed by washing with water and ethanol. For each measurement, 10 μL of catalyst ink (containing 0.75 μg of Pd) was dropped on the cleaned GC electrode and dried at room temperature.

In our discussion, unless otherwise specified, all potentials were measured with reference to RHE. The GC electrode was first cycled in an Ar-saturated $HClO_4$ solution (0.1 M) between 0.08−0.8 V at 100 mV s^{-1} for 20−30 cycles until a stable cyclic voltammetry (CV) curve was obtained. The electrode was then cycled in an Ar-saturated solution containing 0.5 M $HClO_4$ and 0.5 M HCOOH between 0.05–1 V at a scan rate of 50 mV s^{-1} until the current density reached a stable value. Afterwards, the FAO activity test was carried in the same electrolyte between 0.05–1 V at a scan rate of 50 mV s^{-1} for five cycles. All anodic polarization curves displayed were collected from the second cycle. Cu UPD was carried out right after the activity measurement to obtain the electrochemical active surface area (ECSA). The electrode was cycled in an Ar-saturated 0.05 M H_2SO_4 solution between -0.48–0.24 V_{SCE} for 20 cycles at 100 mV s^{-1}, and Cu UPD was then conducted in an Ar-saturated solution containing 0.05 M H_2SO_4 and 0.002 M $CuSO_4$. The potential was held at 0.156 V_{SCE} for 100 s before collecting the UPD curve by linearly

scanning the potential from 0.156 to 0.4 V_{SCE} at a scan rate of 10 mV s^{-1}. The ECSA was calculated by integrating the stripping charge of Cu UPD, assuming a charge of 420 μC cm^{-2} for Pd(100) surface. The data for FAO activity and Cu UPD were corrected by 85% iR compensation (the compensation for the voltage drop between working electrode and reference electrode).

***In situ* Infrared Spectroscopy Measurements.** ATR-IR spectroscopy studies were carried out on a Nicolet iS50 FT-IR spectrometer equipped with a Mercury-Cadmium-Telluride (MCT) detector cooled with liquid nitrogen. A Au-coated Si hemispherical prism (20 mm in diameter, MTI Corporation) was used as the conductive substrate for the catalyst and IR reflection element.[32] A graphite rod and a Ag/AgCl electrode served as the reference and counter electrodes, respectively. A suspension of free-standing Pd-$PdH_{0.706}$ nanocubes (*ca*. 2 mg mL^{-1}) was directly dropped and dried on the Au-coated Si to give a catalyst loading of *ca*. 70 μg cm^{-2}. Real-time ATR-IR spectra of FAO were recorded while linearly sweeping the potential of the working electrode from 0.05 to 1.1 V in an Ar-saturated solution containing 0.5 M $HClO_4$ and 0.5 M HCOOH at a rate of 5 mV s^{-1}. The spectrum collected at 0.1 V served as the reference. Every collection took 10 s (44 scans) at a resolution of 8 cm^{-1}. The CO stripping spectra were then collected by directly purging CO into the solution without altering the optical setup. After CO saturation, the potential of the working electrode was kept at 0.1 V for 10 min to allow for the adsorption of CO. Argon was subsequently purged into the solution for 10 min to remove the dissolved CO while the potential was kept at 0.1 V. Real-time ATR-IR spectra were then recorded while linearly sweeping the potential of the working electrode from 0.1 to 1.1 V at a scanning rate of 5 mV s^{-1}. The spectrum collected at 1.1 V was used as the reference. Every collection took 10 s (44 scans) at a resolution of 8 cm^{-1}. The spectrum was labeled according to the end potential of each scan.

Instrumentation. Transmission electron microscopy (TEM) images were taken using Hitachi HT7700 with an acceleration voltage of 120 kV. The samples were prepared by drop-casting the nanoparticle dispersion on carbon-coated copper grids and dried under ambient conditions. X-ray diffraction (XRD) patterns were obtained on Panalytical XPert PRO Alpha-1 with Cu-Kα radiation. For the samples stopped at 1 V, the working electrode with catalyst went through the FAO anodic scan and was stopped at 1 V. The GC electrode was then sonicated in ethanol to obtain the catalyst subjected to 1 V overpotential. Such a procedure was repeated until an enough amount of catalyst powder (2−3 mg) was obtained for XRD analysis. *In situ* heating XRD was carried out on Panalytical Empyrean. X-ray photoelectron spectroscopy (XPS) data were collected on a Thermo

K-Alpha spectrometer. The high-resolution scanning transmission electron microscopy (STEM) images and the energy-dispersive X-ray spectroscopy (EDX) data were captured using Hitachi HD 2700 with an acceleration voltage of 200 kV. The concentrations of Pd nanocubes were determined using ICP-MS (NexION 300Q, PerkinElmer). Electron energy-loss spectroscopy (EELS) analysis was performed using monochromated, aberration-corrected Nion UltraSTEM 100, operating at an acceleration voltage of 60 kV. It was possible to routinely probe at 1 Å spot size with high convergence angles due to aberration correction up to the fifth order while monochromation enabling a routine energy resolution of 10 meV. The probe convergence semi-angle (α) was 35 mrad, and spectrometer collection semi-angle (β) was 25 mrad. An energy dispersion of 0.05 eV per channel was used to record low-loss spectra, while 0.4 meV per channel was used to record vibrational-loss spectra. The exposure time for the low-loss spectrum was 15 s, while that for the vibrational-loss spectrum was 60 s. A power-law background model was fit to and subtracted from the spectrum to isolate spectral features from the background of the zero-loss peak (ZLP) tail. The spectra were calibrated by setting the maximum of the ZLP to 0 eV. The error in measuring energy was the channel width, *i.e.*, ±0.05 eV for the low-loss spectrum and ±0.4 meV vibrational-loss spectrum.

Computational Methods. Calculations were carried out using the Vienna Ab initio Simulation Package (VASP).[33, 34] Projector augmented wave (PAW) potentials were used to describe the core electron interactions and a 400 eV energy cut-off was employed for the plane-wave basis set. The revised version of the Perdew, Burke, and Ernzerhof (RPBE) exchange-correlation functional[35] was used. Dispersion interactions were accounted for by including the Grimme-D3 semiempirical dispersion corrections.[36] The first Brillouin zone was sampled with a (6 × 6 × 1) Monkhorst−Pack k-point mesh. Geometry optimizations were performed until the Hellman-Feynman forces on each atom were less than 0.03 eV $Å^{-1}$.

A 3 × 3 periodically repeated supercell comprised of six layers was obtained by cutting bulk Pd along the [100] direction. The bottom three layers were fixed at the optimized bulk lattice constant of Pd (3.913 Å), which is in good agreement with the experimental value of 3.89 Å.[37] We utilized a series of slab models to rationalize the effect of hydride phase on the activity toward FAO. In particular, to simulate the hydride phase enrichment observed when increasing the concentration of N_2H_4 in the materials synthesis, we added an increasing number (1−5) of PdH atomic layers on top of the Pd(100) extended surface model. The PdH layers were constructed by

saturating the octahedral sites of Pd(100) with hydrogen. Further, a simplified model for pure $PdH_{0.706}$ was constructed by completely saturating the octahedral sites of the Pd(100) extended surface model with hydrogen atoms. In modelling the $PdH_{0.706}$ phase, we adopted the $PdH_{0.75}$ model phase with the bottom three layers of the slab fixed at the optimized lattice constant of bulk material (4.155 Å), which is in good agreement with the experimental value of 4.059 Å for the $PdH_{0.75}$ phase.[38, 39] The construction of this model avoids the use of excessively large unit cells needed to capture the $PdH_{0.706}$ stoichiometry, while still providing useful insights for rationalizing the effect of Pd-hydride phases on the reactivity at an affordable computational cost. Details on the calculation of onset potentials and other energy-related descriptors can be found in the Supporting Information.

RESULTS AND DISCUSSION

Figure S1 shows a TEM image of the Pd nanocubes, which were synthesized with an average edge length of 15.8 nm using a previously published protocol.[30] The nanocubes were then loaded on carbon black, followed by treatment with aqueous N_2H_4 at different concentrations to obtain Pd-$PdH_{0.706}$/C catalysts with different degrees of β-hydride formation. The crystal phase of the product was determined by XRD. As shown in Figure 1, the emergence of $PdH_{0.706}$ phase was indicated by the appearance of a new peak ($2\theta = 38.7^{o}$, JCPDS No. 18-0951) next to the Pd(111) peak ($2\theta = 40.1^{o}$, JCPDS No. 46-1043). The lattice constants of the Pd and PhH phases in samples obtained under different reaction conditions were calculated using JADE software (Table S1). When the concentration of hydrazine was relatively low (1.8 and 3.9 mM), the lattice constants of the β-hydride phase were smaller than the lattice constant reported for $PdH_{0.706}$ (4.02 Å). As the concentration of N_2H_4 was increased, the lattice constant of the β-hydride phase became essentially identical to the standard value reported for $PdH_{0.706}$. Unlike most of the prior studies, where the entire nanoparticle was converted to the hydride phase,[18, 22, 23, 29, 40] we could control the fraction of $PdH_{0.706}$ in each nanocube by adjusting the concentration of N_2H_4 used in the treatment. For the sample treated with 0.46 mM N_2H_4, there was essentially no change to the crystal phase relative to pristine Pd due to the low concentration of H_2 derived from the decomposition of hydrazine. When the concentration of N_2H_4 was increased, the intensity of the characteristic peak of $PdH_{0.706}$(111) would start to increase at the expense of the Pd(111) peak. For the samples obtained with N_2H_4 concentrations up to 9.2 mM, the peaks corresponding to Pd and $PdH_{0.706}$ always co-

existed. Based on the phase diagram of Pd-PdH reported in the literature,[41] the atomic H/Pd ratio of 0.706 is already well into the pure β-hydride region, eliminating the possibility to detect both α and β phases. Therefore, we believe that each particle in the Pd-PdH sample should be viewed as a mosaic of Pd and $PdH_{0.706}$ regions.

The transformation should involve the following reactions:

$$N_2H_4 \xrightarrow{Pd} N_2 + 4\,H \quad (1)$$

$$xH + Pd \longrightarrow PdH_x \quad (2)$$

The H atoms that were not inserted into the Pd lattice then combined to form H_2:

$$2H \longrightarrow H_2 \quad (3)$$

Due to the presence of a trace amount of the residual capping agent (PVP or Br^-) on the surface, the H atoms would prefer to diffuse into the Pd lattice from edges populated by vacancy sites, quickly generating $PdH_{0.706}$ in the accessible volume. Afterwards, the H atoms had to diffuse at a slower speed to further increase the degree of hydride formation. Meanwhile, the residual capping agent could desorb from the side faces, generating additional vacancy sites for the uptake of more H atoms.

Although Pd can, in principle, adsorb hydrogen to give PdH_x with x varying from 0 to 1, it is unlikely that our product was composed of PdH_x nanocubes with a gradient in composition across each particle to give an average value of 0.706 for x. Otherwise, we would expect to observe a continuous shift to the major XRD peak from $2\theta = 40.1^o$ (for Pd) to $2\theta = 38.1^o$ (for $PdH_{0.706}$), rather than the two distinct peaks representing Pd and $PdH_{0.706}$ with variable intensities as the degree of hydride formation was increased. The same method could also be extended to Pd nanocrystals with other shapes such as octahedra terminated in {111} crystal facets (Figure S2), indicating the generality of this method. In the current system, the favorable occupation of about 70% of the available octahedral sites by H atoms can be attributed to the "electronic saturation" rather than "crystallographic saturation". It was reported that the paramagnetic susceptibility of PdH_x would drop to zero when x approached 0.7, corresponding to the complete filling of the 4d band of Pd.[42]

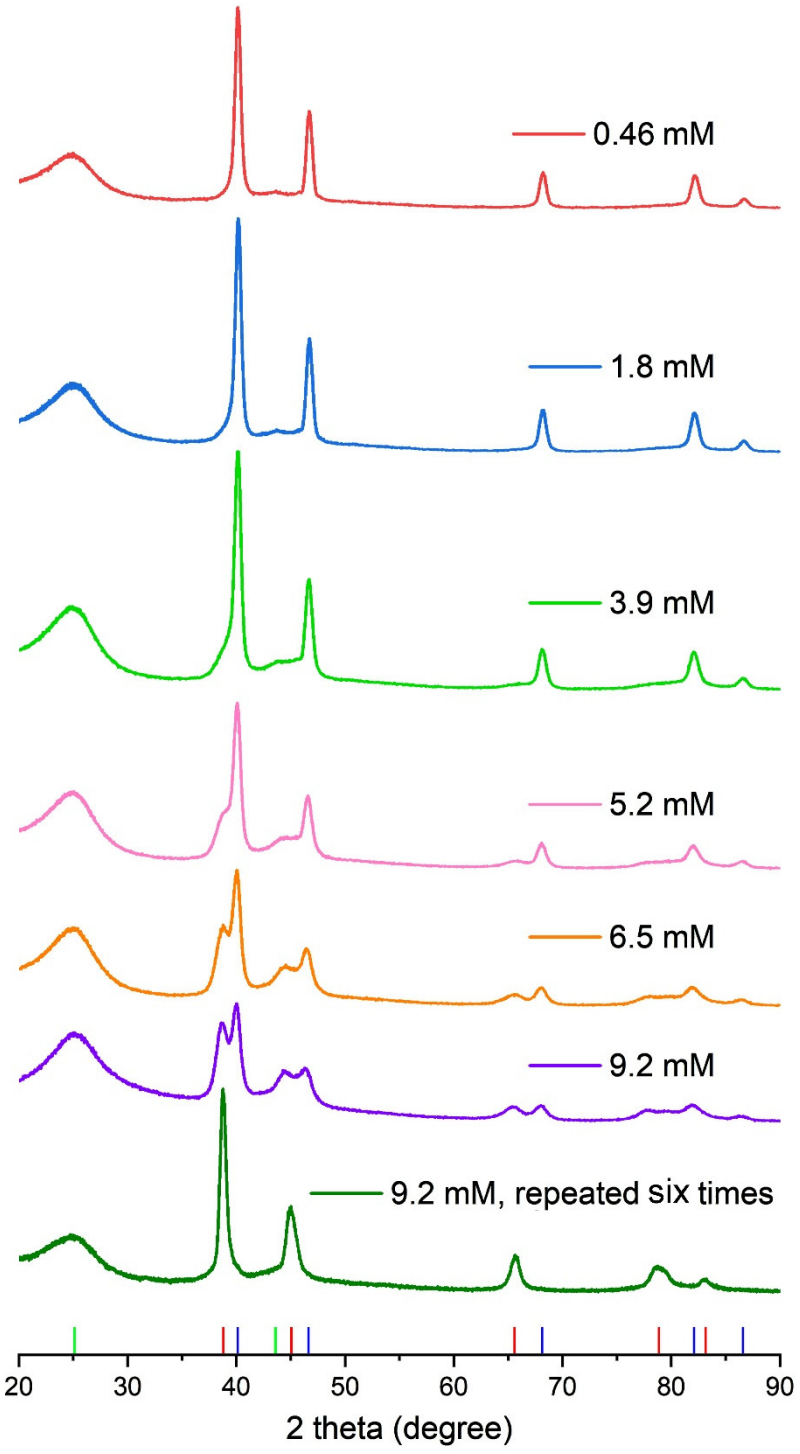

Figure 1. XRD patterns recorded from different Pd-$PdH_{0.706}$/C catalysts. The number above each pattern represents the concentration of N_2H_4 in the solution used for treating the Pd nanocubes. The blue, red, and green bars on the x axis indicate the standard diffraction peaks of *fcc*-Pd, $PdH_{0.706}$, and carbon black (Vulcan XC72), respectively.

Since the XRD data could only tell us the degree of lattice expansion rather than the elemental composition of the sample, we performed EDX, EELS, and XPS analysis to exclude the possible formation of carbide or nitride and further confirm the presence of H atoms in the Pd lattice. First of all, the formation of carbide can be excluded since N_2H_4 does not contain any carbon atom. The possible involvement of the C atoms from PVP or carbon support could also be excluded since we did not observe any change to the samples obtained with N_2H_4 up to 0.46 mM, despite the presence of carbon support and PVP (Figure 1). Secondly, the formation of nitride could be excluded based on the EDX data shown in Figure S3, a and b. Compared with the signals from Pd, the signals from N were too weak to account for the lattice expansion observed in the XRD patterns. If the samples were PdN_x nanocubes, the EDX signals from N should be much stronger and they should also be spatially registered with those from Pd.[43] Thirdly, the formation of hydride was further confirmed by EELS analysis. It is worth pointing out that the current of the monochromated electron beam used in the analysis was low enough to avoid knocking out hydrogen from the specimen. Figure S3c shows the annular dark-field image recorded from a number of $PdH_{0.706}$ nanocubes. One of the nanocubes was subjected to EELS analysis, with the position of the electron beam used for data acquisition marked by a star. Figure S3d shows the corresponding energy-loss spectra, before and after background subtraction. The acquired spectrum is in good agreement with the previously reported STEM EELS data collected from PdH thin films.[44] The spectral position of the peak closest to the ZLP was 6.84 eV (inset in Figure S3d), corresponding to the electronic transition of PdH solid.[45] The pristine Pd nanocubes showed a peak around 7.29 eV, which was shifted to 6.84 eV upon complete conversion to $PdH_{0.706}$. Another evidence in support of hydride formation came from the vibrational STEM-EELS spectra in Figure S3, e-g. When the probe was directly positioned on the nanocube (Figure S3, e and g), we observed a well-defined peak between 50-60 meV, corresponding to the local modes of H atoms vibrating in the octahedral sites of Pd lattice.[46, 47] In contrast, when we switched to the "aloof mode" to probe the surface contamination (Figure S3, f and g), no peak was resolved between 50-60 meV, despite the presence of PVP (as indicated by a broad peak extending from 120-210 meV).[48] The formation of hydride was further supported by the XPS valance band spectra (Figure S4). The valence band of the $PdH_{0.706}$ sample showed three characteristic features of PdH_x: *i*) the decrease in bandwidth by 10% relative to that of the Pd sample, as a result of the increase in distance between Pd and Pd atoms;[49] *ii*) the

appearance of a small peak between 6-7 eV, corresponding to the interaction between Pd 4d orbital and H 1s orbital;[50] and *iii*) the shifting of peak away from the Fermi level because of the reduced density at Fermi energy as caused by the insertion of H atoms into Pd lattice.[51] These observations are consistent with what are reported in the literature regarding the formation of hydride.[18, 22, 52]

Interestingly, when we further increased the concentration of N_2H_4 to 13 mM and higher, we no longer detected the formation of hydride phase (Figure S5). The nanocubes could only be completely converted from Pd to $PdH_{0.706}$ by consecutively treating the same sample with 9.2 mM N_2H_4 multiple times. This unexpected result urged us to further analyze the reaction parameters that could potentially affect the formation of $PdH_{0.706}$ (Figure S6). By varying the pressure in the vial while maintaining the concentration of both Pd nanocubes and N_2H_4, we found that the initiation of phase transformation would only occur when the pressure of H_2 was lower than 17.6 kPa (Figure S6a and Table S2). One possible explanation is that the decomposition products of N_2H_4 is dependent on its concentration. When the concentration of N_2H_4 goes above a threshold value, the generation of H atoms would stop. Moreover, the degree of hydride formation was also dependent on the ratio of $n(H_2)$ to n(Pd) (Figure S6b). Therefore, if we want to achieve a scale-up synthesis in a batch reactor, the mass of the nanocrystals and the volume of the reactor should be enlarged at the same proportion to maintain a constant H_2 pressure, while keeping the $n(H_2)$/n(Pd) ratio unchanged. Besides pressure, we found that the degree of hydride formation relied on the reaction temperature and reaction time (Figure S6, c and d). The dependence on temperature could be explained by the variations in N_2H_4 conversion at different temperatures,[53] while the time dependence indicated that the rate determining step in the formation of $PdH_{0.706}$ by N_2H_4 treatment was likely the decomposition of N_2H_4 to generate H atoms or the creation of surface vacancies to allow the H atoms to diffuse into the Pd lattice.

It is worth pointing out that the as-prepared Pd-$PdH_{0.706}$/C catalysts were all free of secondary contamination and stable under ambient conditions without showing any change in phase composition for at least four months (Figure 2a). It has been reported in a number of studies that the PdH_x samples derived from organic compounds such as DMF and $NaBH_4$ in a solution phase were more stable at room temperature than those prepared using H_2 in a gas phase.[21, 22] When the support-free $PdH_{0.706}$ nanocubes were heated to higher temperatures under the protection of N_2, the *in situ* XRD indicated that the hydride phase could be retained up to 150 °C. As the temperature reached 200 °C, a transformation from $PdH_{0.706}$ to Pd was initiated and the sample was completely

converted back to Pd at 250 ºC (Figure 2b). At the moment, it is still unclear why the hydride stability had a correlation with the reagent involved in the synthesis. One possible explanation is that when the sample was dried in an oven, the residual PVP could block the vacancy sites on the surface, making it hard for the H atoms inside the lattice to escape under ambient conditions. It was reported that PVP would start to decompose around 200 ºC,[54, 55] allowing the absorbed H to escape and thus triggering the phase transformation from $PdH_{0.706}$ to Pd. Besides the reagents involved in the synthesis, the thermal stability of the hydride was also found to be dependent on the atmosphere. Table S3 shows a comparison of the conditions used for the preparation of PdH_x, along with their thermal stability observed in different atmospheres. It can be seen that the presence of H_2 gas would facilitate the desorption of H from the Pd lattice, compromising the thermal stability of the hydride sample. If the hydride sample was annealed in an atmosphere free of H_2, it tended to exhibit enhanced thermal stability.[56] In the presence of Pd surface, the decomposition products of N_2H_4 are N_2 and H_2, and none of them should cause secondary contamination.[53] Furthermore, the N_2H_4 solution was used at a relatively low concentration and mild reaction temperature, greatly minimizing potential safety risk.[57] Different from N_2H_4, both DMF and $NaBH_4$ generate other species that can potentially adsorb on the particle surface and the syntheses typically require the use of a higher temperature and/or pressure that may cause safety concerns.[22]

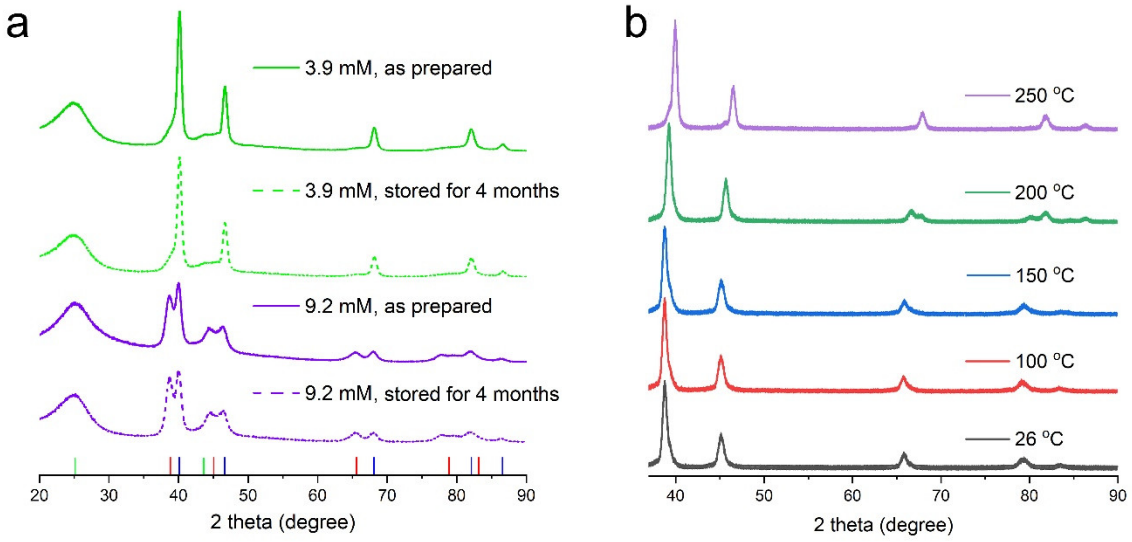

Figure 2. (a) XRD patterns of the as-prepared Pd-$PdH_{0.706}$/C catalysts and the same samples after storage under ambient conditions for four months. The number above each pattern represents the concentration of N_2H_4 solution used for the treatment. (b) XRD patterns of support-free $PdH_{0.706}$

catalysts heated *in situ* to different temperatures under N_2 atmosphere. The blue, red, and green bars above the horizontal axis indicate the standard diffraction peaks of *fcc*-Pd, $PdH_{0.706}$, and carbon black (Vulcan XC72), respectively.

Electron microscopy analysis was applied to further resolve the spatial distribution of $PdH_{0.706}$ phase within each nanocube. Figure 3, a-d, shows the representative TEM images of four Pd-$PdH_{0.706}$/C catalysts with increasing contents of $PdH_{0.706}$. The heating and formation of $PdH_{0.706}$ did not affect the overall morphology as the particles in all samples still showed a cubic shape after the treatment. However, as shown by the images in the insets, there was an obvious change to the contrast displayed by different regions of an individual nanocube, which can be attributed to the diffraction contrasts arising from two phases with different lattice constants.[27] As the concentration of N_2H_4 was increased, the formation of $PdH_{0.706}$ tended to start from the edge/corner site(s) and then propagate to the bulk of the nanocube. The results from our *ex situ* characterizations are in agreement with previous studies involving *in situ* TEM and X-ray diffractive imaging of Pd nanocubes when they were exposed to H_2 gas.[25, 27] Based on the contrast displayed in the TEM images, the Pd-$PdH_{0.706}$ nanocubes did not take a core-shell structure by forming a complete $PdH_{0.706}$ shell over the entire surface. Instead, each particle was comprised of a mix of both $PdH_{0.706}$ and Pd regions. Although the $PdH_{0.706}$ nanocubes in Figure 3d showed round edges/corners as a result of multiple rounds of heating treatment, the surface of each nanocube was still terminated in smooth {100} facets, as confirmed by the STEM images in Figure S7.

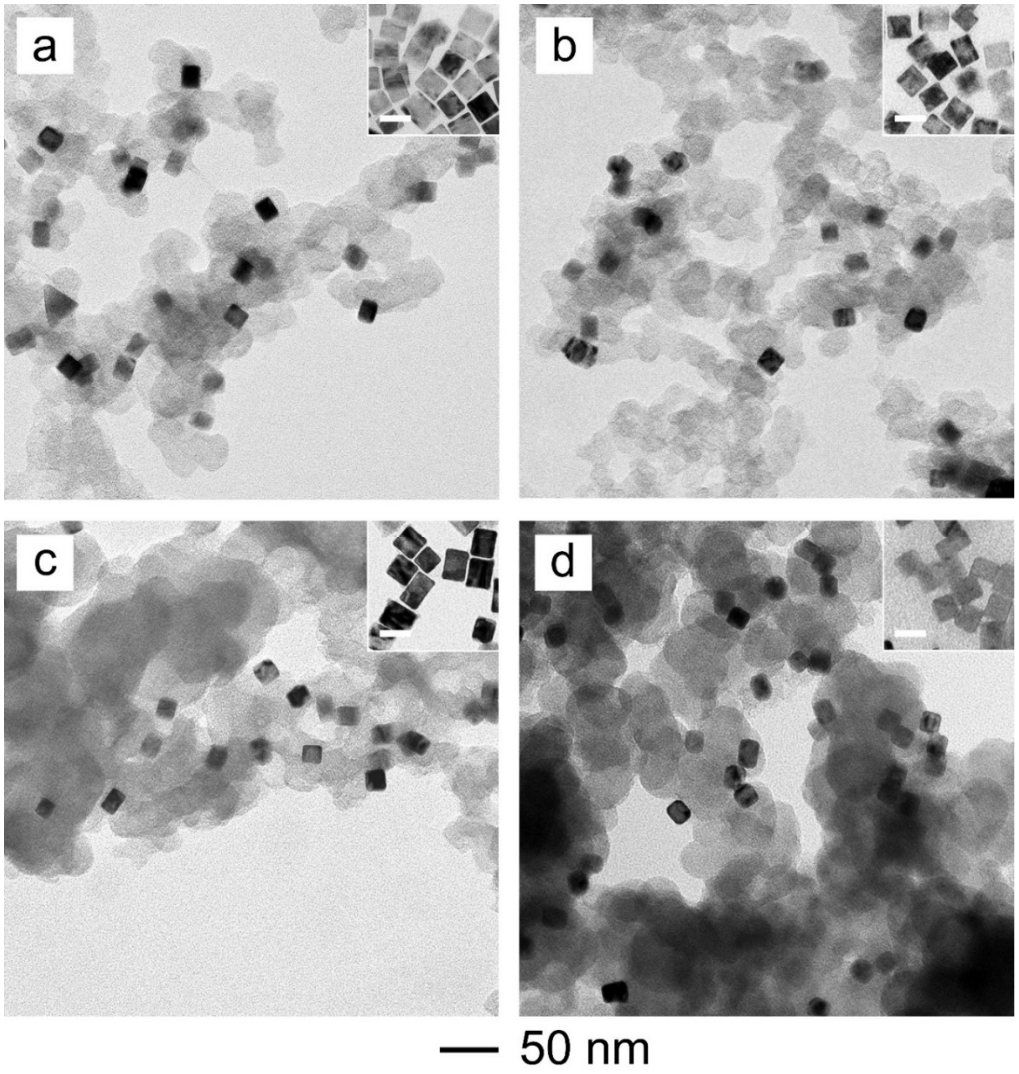

Figure 3. TEM images of Pd nanocubes supported on carbon black after treating with aqueous N_2H_4 at different concentrations: (a) 1.8, (b) 3.9, and (c) 9.2 mM, respectively. The sample shown in (d) was repeatedly treated with 9.2 mM N_2H_4 six times. The insets show the free-standing Pd nanocubes that went through the same treatments (scale bars: 20 nm).

Since the treatment process did not involve additional colloidal stabilizer or organic solvent, the surface of the catalyst should not suffer from secondary contamination, making it advantageous for a variety of catalytic applications. It is expected that the change in lattice constant and thus the induced surface strain, as well as the possible defects introduced by H incorporation, would alter the surface and catalytic properties of the Pd nanocubes. To this end, we used FAO as a probe reaction to investigate and compare the catalytic properties of $Pd_{nanocube}/C$, Pd-$PdH_{0.706}/C$, and $PdH_{0.706}/C$. Figure 4 shows the anodic scans of different catalysts in an Ar-saturated electrolyte

containing HCOOH and $HClO_4$. As reported in our previous study, the addition of a trace amount of N_2H_4 during the heating process could remove the Br^- capping layer without destructing the surface structure of the nanocube, leading to enhancement in current density at 0.4 V toward FAO.[15] When increasingly transforming the nanocubes from Pd to $PdH_{0.706}$, we firstly observed a volcano trend for the catalytic activity of Pd-$PdH_{0.706}$/C. As illustrated in Figure S8, both the peak current density and the current density at 0.4 V increased as the concentration of N_2H_4 was increased from 0.46 mM to 3.9 mM, while both current densities started to decrease as the concentration of N_2H_4 was further increased to 5.2, 6.5, and 9.2 mM. Significantly, when the Pd nanocubes were fully converted to $PdH_{0.706}$, the catalytic performance toward FAO was substantially enhanced. The current densities of $PdH_{0.706}$/C at 0.4V and at peak potential were four and two times as high as those of the pristine Pd nanocubes, respectively. When compared with the previously reported activity of $PdH_{0.43}$ toward FAO,[19] our result demonstrated that $PdH_{0.706}$ was more efficient in catalyzing this reaction. The ECSAs of different catalysts are provided in Table S4. The pure $PdH_{0.706}$/C sample has a slightly lower ECSA compared to all other samples, possibly due to the loss of catalyst and possible aggregation of the nanocubes during repeated heating/washing process (see experimental sections for details).

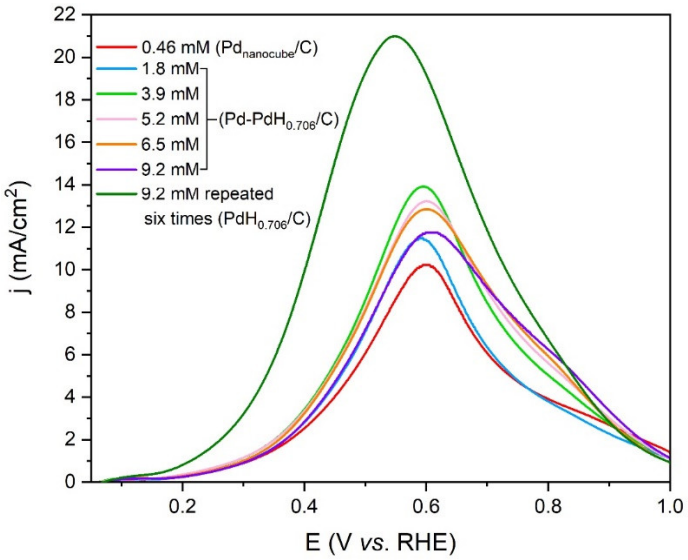

Figure 4. Anodic polarization curves of the $Pd_{nanocube}$/C, Pd-$PdH_{0.706}$/C, and $PdH_{0.706}$/C catalysts, with the current densities normalized to the ECSA. The measurements were carried out in an Ar-saturated electrolyte containing 0.5 M $HClO_4$ and 0.5 M HCOOH.

More details about the surface and bulk structures of the Pd-$PdH_{0.706}$/C catalysts were further obtained by analyzing the CV traces and Cu UPD curves. Figure S9 shows changes to the CV and Cu UPD curves as the content of $PdH_{0.706}$ in the catalyst was increased. According to a previous study, the peaks between 0.12−0.3 V correspond to the underpotential deposition of H while the sharper peaks located in the range of 0.05−0.12V are related to H absorption into the bulk Pd lattice.[58] As the concentration of N_2H_4 was increased from 0.46 mM to 6.5 mM, there was a major increase in the H absorption peak, suggesting easy penetration of H into the bulk of the particle. This result could be ascribed to the expansion of the Pd lattice caused by its neighboring $PdH_{0.706}$ domains, making it easier for H to transport into the bulk. As the content of $PdH_{0.706}$ was further increased, fewer "expanded empty sites" would be left behind for H to go to, and the area of the H absorption peak started to decrease. Similarly, from the Cu UPD curves, we also observed that the peak corresponding to the oxidation of Cu UPD gradually shifted from 0.25 to 0.225 V_{SCE} as the content of $PdH_{0.706}$ in the nanocubes was increased. This trend indicates that the interaction between the Cu and Pd atoms was weakened as the crystal structure changed from Pd to $PdH_{0.706}$.

We believe these electrochemical features are correlated with the surface structure of the Pd-$PdH_{0.706}$ catalyst and can be used to evaluate the stability of the crystal structure during the reaction. The stability of the crystal structure during FAO is one of the key issues in interpreting the structure-catalytic property relationship. Using the Pd-$PdH_{0.706}$/C catalyst obtained from one-time treatment in 9.2 mM N_2H_4 as an example, Figure 5, a and b shows the XRD patterns and Cu UPD curves that were recorded before FAO and during FAO at the highest potential (*i.e.*, 1.0 V), respectively. There was essentially no change to the relative intensity between the major XRD peaks of Pd and $PdH_{0.706}$, indicating that the $PdH_{0.706}$ phase could be fully retained even at the highest potential for FAO. We also calculated the lattice constants of the phases in the samples shown in Figure 5a using JADE software (Table S5), further confirming the stability of the crystal structure before and after applying the potential. Similarly, the two Cu UPD patterns showed an almost identical main peak at 0.25 V_{SCE}, with a large shoulder peak at 0.225 V_{SCE}. Since the catalyst stayed stable at the highest potential applied, it can be concluded that the $PdH_{0.706}$ phase was robust and stable not only under ambient conditions but also during the FAO reaction. Figure 5c shows TEM image of the catalyst after going through the electrocatalytic reaction. Again, there was no obvious changes to the shape and dispersion state of the nanocubes.

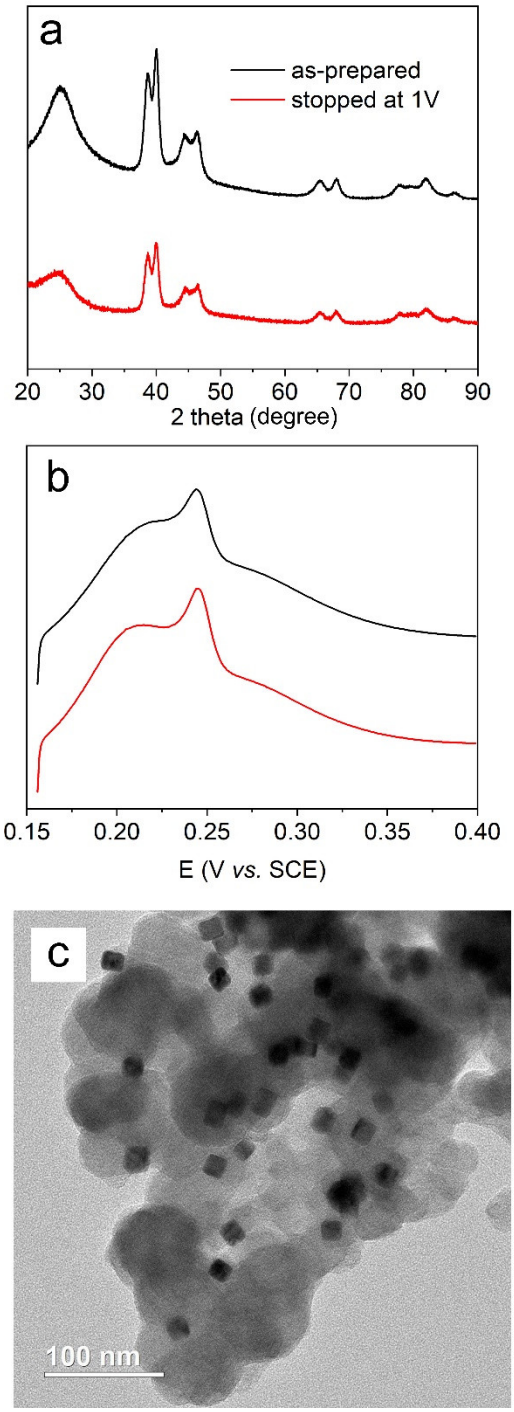

Figure 5. (a) XRD patterns and (b) Cu UPD curves recorded from the Pd-$PdH_{0.706}$/C catalyst (treated once with 9.2 mM N_2H_4 solution) and the same catalyst after stopping the CV cycling at 1.0 V of overpotential. (c) TEM image of the same catalyst post FAO test.

To gain a deeper insight into the structure-property relationship of the $PdH_{0.706}$ nanocubes, we also carried out stability test and evaluated the dependence the FAO activity on the pH of the electrolyte. Figure S10a shows the anodic polarization curves of the $PdH_{0.706}$/C catalyst before and after 1,500 cycles in 0.1 M $HClO_4$. Despite a major decrease in the peak current density, the peak potential was found to shift toward lower values during the stability test. As a result, there was almost no change to the current density at 0.4 V (Figure S10b), making the catalyst interesting for commercial DFAFCs. Moreover, no severe aggregation or shape deformation was observed for the catalytic particles, as confirmed by the TEM image (Figure S10c) and Cu UPD curve (Figure S10d) of the catalyst after the stability test. The peak position of the Cu UPD curve was still located at 0.22 V_{SCE}. Since the peak position is sensitive to the crystal structure of the nanocubes (Figure 5 and Figure S9), this observation supports our claim that the $PdH_{0.706}$ catalyst remained in the β-hydride phase during the stability test. On the other hand, the FAO performance of the catalyst was found to be highly dependent on the pH of the electrolyte. When the concentration of $HClO_4$ in the solution was increased, the pH and the peak current density both decreased. Meanwhile, a negative shift in peak potential was also observed, thereby keeping the current densities at 0.4 V essentially unchanged (Figure S11a). The pH was also found to affect the stability of the catalyst. When the concentration of $HClO_4$ was increased, the current density would decrease more quickly even within the first ten cycles (Figure S11b). Taken together, the pH of the electrolyte should be optimized to ensure and maintain a relatively high current density at 0.4 V, as well as long-term stability for the catalyst.

The strain field observed in TEM images and the "volcano type" catalytic activity remind us of the well-known geometric effect in bimetallic catalysts, where the strain induced by the lattice mismatch is dependent on the overlayer thickness.[59] To this end, we employed first-principles DFT calculations to shed light on the effect of the hydride overlayer thickness on the FAO reaction mechanism. To rationalize the effect of hydride phase on the activity toward FAO, we utilized a series of slab models, as shown in Figure S12. The free energy diagram (FED) for the FAO reaction on Pd-PdH slab models, with 1-, 3-, and 5-PdH overlayers, is reported in Figure 6a-c, with the same analysis for Pd(100), 2-, and 4-PdH overlayers being reported in Figure S13. FAO can proceed through two main pathways, namely formate (HCOO) and carboxyl (COOH), with the latter potentially leading to the formation of CO on the surface. Therefore, the energy difference between HCOO* and COOH* ($\Delta_{HCOO-COOH}$), where * denotes a reaction intermediate adsorbed on

the surface, can be used as a descriptor for the selectivity of the catalyst toward one of these two pathways. We found that $\Delta_{HCOO\text{-}COOH}$, reported in Figure 6 and Table 1, was sensitive to the thickness of the PdH overlayer included in the models. In particular, COOH* is more stabilized (positive values of $\Delta_{HCOO\text{-}COOH}$) on bare Pd(100) extended surface (Figure S13a) and when 1 or 5 layers of PdH are supported on Pd(100). In these cases (Figure 6, a and c, respectively), the formation of CO* from COOH* was preferred over COOH's dehydrogenation. Instead, HCOO* was preferred over COOH* (negative values of $\Delta_{HCOO\text{-}COOH}$, see Table 1) when PdH overlayers of 2, 3, or 4 layers thick are supported on top of the Pd(100) surface. In particular, HCOO* was stabilized the most on the PdH overlayer of 4 layers thick, with $\Delta_{HCOO\text{-}COOH}$ = -0.19 eV. This trend is reminiscent of the activity trend observed in Figure 4, suggesting that a narrow range of PdH overlayer thicknesses exist where HCOO* is stabilized over COOH*, leading to reduced CO* poisoning and increased FAO activity. Furthermore, since the water activation step ($H_2O_{(g)} \rightarrow OH^* + 1/2H_{2(g)}$) on all Pd-PdH models is highly endergonic (see Table 1), we can exclude that CO* could be converted to CO_2 *via* indirect oxidation pathways that involve CO* and OH* reaction.

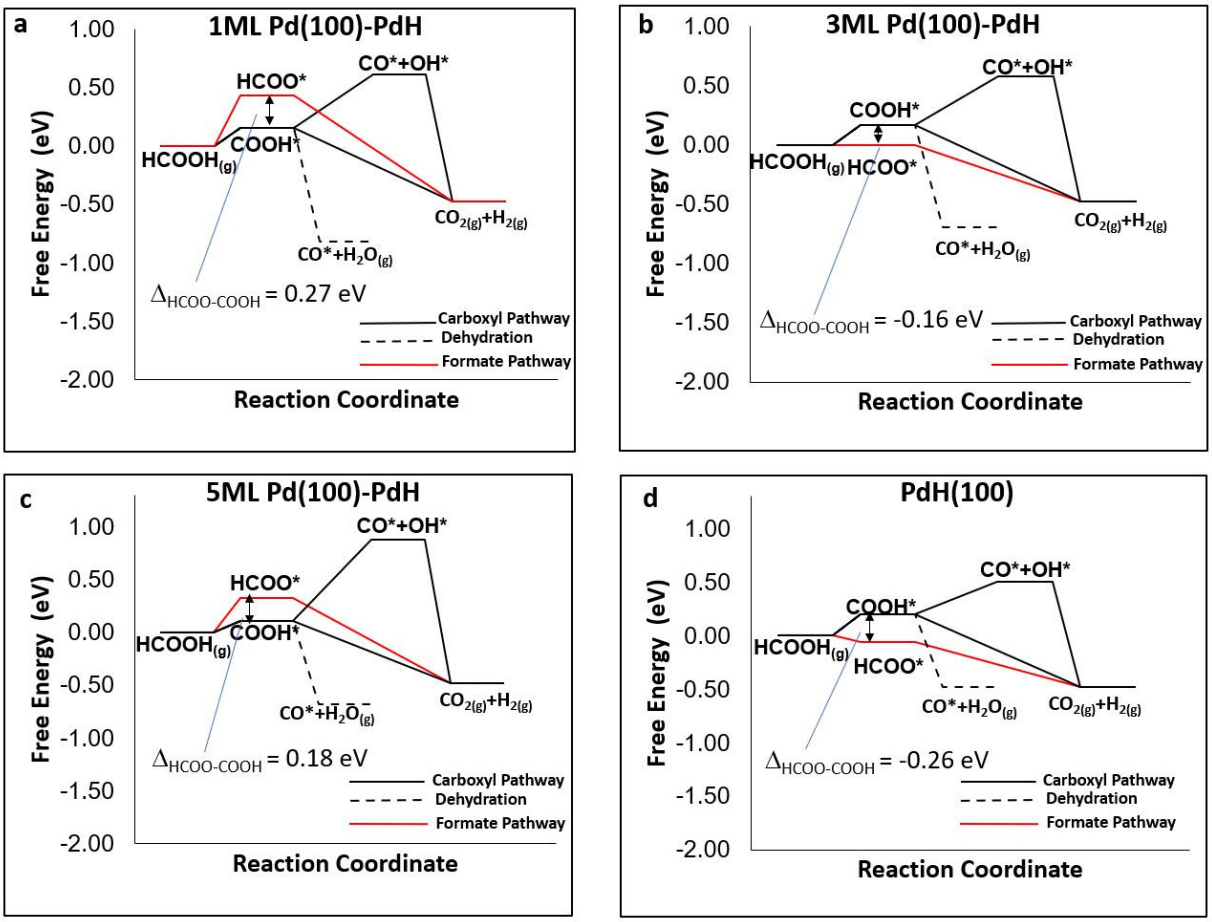

Figure 6. Calculated free energy diagrams for FAO on the Pd-PdH slab models with varying overlayer thickness at 0.0 V: (a) 1 monolayer (ML) of PdH; (b) 3 ML of PdH; (c) 5 ML of PdH; and (d) a pure PdH(100) bulk model. Black lines indicate the carboxyl pathway of FAO, proceeding either through dehydrogenation (solid lines) or dehydration (dashed lines). Red lines indicate the formate pathway. Stoichiometry is balanced with H^+ and e^-, which are not shown explicitly. $\Delta_{HCOO\text{-}COOH}$ indicates the energy difference between adsorbed HCOO* and adsorbed COOH*. Positive (negative) values indicate preferential stabilization of COOH*(HCOO*).

The predicted onset potentials in Table 1 also reflect a non-monotonic trend of activity as a function of the PdH overlayer thickness. Among the models considered, the one presenting a PdH of three atomic layers is the most active, with an onset potential of 0.04 V. The limiting cases involving one and five atomic layers show higher onset potentials (0.16 and 0.15 V, respectively), in qualitative agreement with the volcano-trend observed in Figure 4. We note here that a quantitative agreement between experimental and computationally-predicted onset potential

would be very challenging as our model ignores surface coverage of various reaction intermediates and solvent effects, and only approximately describes the effect of the external applied potential. Finally, we analyze the case of PdH(100) as a model for nanocubes made of pure $PdH_{0.706}$. The FED for FAO on PdH(100) is shown in Figure 6d. Interestingly, the first $HCOOH_{(g)}$ dehydrogenation step through the formate-mediated pathway was exergonic. Instead, as demonstrated by the onset potentials reported in Table 1, the first dehydrogenation step for the Pd-PdH slab models, through either the formate- or carboxyl-mediated pathway, was always potential-determining. This is an indication of the higher activity of electrocatalyst models made of pure PdH with respect to the Pd-PdH ones, in qualitative agreement with the electrocatalyst activity trend experimentally observed. We propose that this trend is due to the release of the compressive strain which was exerted on PdH by the underlying Pd lattice, in the case of Pd-PdH models. Furthermore, the preferential stabilization of HCOO* over COOH* on PdH(100), would explain the high selectivity of PdH toward CO_2 and H_2, with negligible CO formation.

Table 1. Activity and selectivity descriptors obtained from DFT calculations. For FED downhill in energy at 0 V (Pd(100) and PdH(100)), the predicted onset potential is indicated by a double dash (--). $\Delta_{HCOO\text{-}COOH}$ indicates the difference in Gibbs free energy between adsorbed HCOO* and COOH* (positive values indicate preferential stabilization of COOH* over HCOO*, and *vice versa*). ΔG_{CO*} and $\Delta G_{H2O\rightarrow OH*+1/2H2}$ indicates the Gibbs free energy of adsorption of CO* and the reaction energy associated to water activation step, respectively.

	Onset Potential /V	**$\Delta_{HCOO\text{-}COOH}$ /eV**	**Preferred Pathway**	**ΔG_{CO*} /eV**	**$\Delta G_{H2O\rightarrow OH*+1/2H2}$ /eV**
Pd(100)	--	0.19	Carboxyl	-1.76	0.62
1ML Pd(100)-PdH	0.16	0.27	Carboxyl	-0.66	1.43
2ML Pd(100)-PdH	0.14	-0.04	Formate	-0.64	1.36
3ML Pd(100)-PdH	0.04	-0.16	Formate	-0.54	1.29
4ML Pd(100)-PdH	0.05	-0.19	Formate	-0.42	1.32
5ML Pd(100)-PdH	0.15	0.22	Carboxyl	-0.52	1.57
PdH(100)	--	-0.26	Formate	-0.49	1.17

To rationalize the stability and activity trends observed in Figure 6 and Table 1, we calculated the Density of States and performed a Bader Charge analysis on the investigated systems. The density of d-states projected on Pd atoms in the first layer of the slab with increasing PdH overlayer thickness is reported in Figure S14. Irrespective of the number of PdH overlayers, the shape and width of the d-band remains approximately the same. This excludes that the trends observed in the FEDs reported in Figure 6 and the data reported in Table 1 could be rationalized by analyzing the electronic structure of the system. Similar conclusions can be drawn by observing how the energy difference between HCOO and COOH ($\Delta_{HCOO\text{-}COOH}$) depends on the Bader charge of the Pd atoms serving as adsorption site for these two reaction intermediates. In our previous work, we have demonstrated that $\Delta_{HCOO\text{-}COOH}$ strongly depends on the Bader charge localized on Pd atoms,[60] but the data reported in Figure S15 do not suggest any appreciable trend. As descriptors directly depending on the electronic structure of the system did not appear to capture the trends observed in Figure 6, we have used a descriptor-based analysis derived from geometric properties to rationalize the observed trends. In particular, we have employed three Pd–Pd bond lengths: *i*) the bond length between two consecutive PdH layers (LC1); *ii*) the bond length between two Pd atoms defining the edge of a Pd_4 square, within the same PdH layer (LC2); and *iii*) the bond length between two Pd atoms defining the diagonal of a Pd_4 square within the same PdH layer (LC3). A schematic of LC1, LC2, and LC3 is shown in the left part of Figure S16. The data reported in the table section of Figure S16 suggest an inter-layer relaxation of LC1 that can be observed going from 1 ML Pd(100)-PdH to 2 ML Pd(100)-PdH and thicker layers. This relaxation can be related to a higher degree of undercoordination of the Pd sites, which we have previously demonstrated to stabilize HCOO over COOH.[4, 60, 61] With the exception of 5 ML Pd(100)-PdH, the same trend appears to be valid also in this case: on thin and contracted PdH overlayers, COOH is stabilized over HCOO (positive $\Delta_{HCOO\text{-}COOH}$), while the opposite is true for thicker overlayers.

In situ ATR-IR measurements were also carried on support-free Pd and $PdH_{0.706}$ nanocubes to assess the coverage of CO adsorbed on the Pd surface during FAO. Figure 7, a and b shows the potential-resolved ATR-IR spectra for the two samples. We only observed the presence of CO_2 (located around 2340 cm^{-1}) and multiply-bonded CO species (CO_M, located around 1750 cm^{-1}). Relative to the background recorded at 0.1 V, the positive bands indicate the formation of CO_2 with increasing potential, whereas the negative bands stand for the decreasing of CO_M species as the potential went higher. No band associated with CO coordinated in a bridge (CO_B) or linear

(CO_L) geometry was resolved across the entire potential range, indicating that the surface coverage of CO was very low. On the other hand, CO stripping spectra of the same catalyst showed that CO_L, CO_B, and CO_M could all be clearly resolved from the spectra when CO was purged into the solution to enable a full monolayer of surface coverage (Figure 7, c and d). Previous studies suggested that the CO_B band could be detected at a CO coverage as low as 0.03 ML.[62] Therefore, the absence of CO_B and CO_L bands indicated a very low coverage of CO on the surface of $PdH_{0.706}$ nanocubes, validating the preferential oxidation *via* the formate-mediated pathway as predicted by the DFT calculations. Since a low surface coverage of CO was observed throughout the whole potential range (from 0.15 to 1.1 V), it can be concluded that the surface of the $PdH_{0.706}$ remained stable during the entire course of the reaction. If any Pd was exposed on the surface, a stronger CO binding signal should be observed, according to our DFT calculation. At the same time, the low coverage of CO* observed for the Pd nanocubes obtained by treatment with 0.46 mM N_2H_4 suggested that even under this mildly reducing condition, domains of PdH of 2−3 atomic layers in thickness could still form. Such a thin thickness could hardly be detected by XRD analysis, but it was enough to promote oxidation *via* the formate pathway.

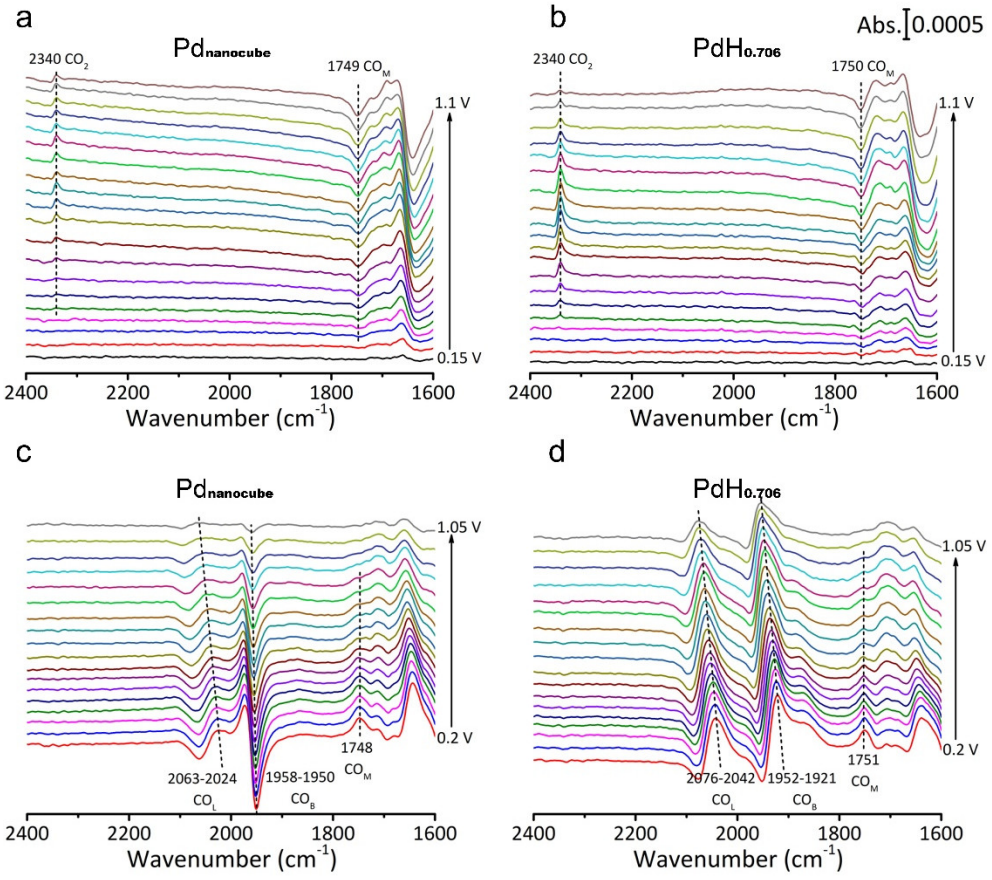

Figure 7. (a, b) *In situ* ATR-FTIR spectra of FAO on (a) Pd nanocubes treated in 0.46 mM N_2H_4 and (b) $PdH_{0.706}$ nanocubes in an Ar-saturated electrolyte containing 0.5 M $HClO_4$ and 0.5 M HCOOH. Reference spectra for (a, b) were taken at 0.1 V. (c, d) *In situ* ATR-FTIR spectra of FAO on (c) Pd nanocubes treated in 0.46 mM N_2H_4 and (d) $PdH_{0.706}$ nanocubes in the same electrolyte but purged with CO before measurement. CO was allowed to absorb on Pd at 0.1 V for 10 min to achieve saturation and thus the formation of a monolayer, and then oxidized by positively scanning the potential to 1.1 V. Reference spectra for (c, d) were recorded at 1.1 V. CO_L, CO_B, and CO_M correspond to CO adsorbed at atop, bridge, and multi-bonded sites, respectively.

CONCLUSION

In summary, we have developed a solution-phase method to transform nanocubes from Pd to $PdH_{0.706}$ with controllable degrees of hydride formation. The success of this synthesis relies on the use of N_2H_4 at a low concentration under mild temperature and pressure. The resulting nanocubes were tested as catalysts toward FAO and the activity was found to be stable and strongly dependent on the elemental composition, with nanocubes made of pure $PdH_{0.706}$ performing the best among all the catalysts. This result is in agreement with DFT calculations, where the thickness of PdH overlayers on Pd(100) in the slab models was found to affect both the predicted onset potential and the preferred FAO pathway. In particular, the stability of HCOO* and COOH* reaction intermediates showed a non-monotonic trend as a function of the PdH overlayer thickness. As a consequence, the carboxyl-mediated pathway was preferred on very thin or thick PdH overlayers, while three atomic layers of PdH showing the best trade-off between activity (low onset potential) and selectivity (preferential formation of CO_2 and H_2). Furthermore, DFT calculations showed that PdH(100), employed as a model for $PdH_{0.706}$, outperformed the Pd-PdH nanocube models, owing to the exergonic FAO and the involvement of the formate pathway. The strategy reported here can be potentially used to fine-tune the activity and selectivity of Pd-based catalysts toward a variety of other reactions without increasing the amount of Pd needed.

ASSOCIATED CONTENT

Author Contributions

†Y. Shi and R. Schimmenti contributed equally to this work.

Notes

The authors declare no competing financial interest.

Supporting Information

TEM images, XRD patterns, EDX line scan, EELS spectra, XPS analysis, and results from electrochemical measurements of Pd, Pd-$PdH_{0.706}$, and $PdH_{0.706}$ samples are provided. Additional calculation details and results are also presented.

Acknowledgement

This work was supported in part by the Department of Energy, Office of Basic Energy Sciences, Catalysis Science Program (grant DE-FG02-05ER15731) and start-up funds from the Georgia Institute of Technology. The electron microscopy, XPS and XRD analyses were conducted at the Institute of Electronics and Nanotechnology (IEN, Georgia Institute of Technology), a member of the National Nanotechnology Coordinated Infrastructure (NNCI), which is supported by the National Science Foundation (ECCS-2025462). Part of the computational work was carried out using supercomputing resources at National Energy Research Scientific Computing Center (NERSC). NERSC is supported by the U.S. Department of Energy, Office of Science, under contract DE-AC02-05CH11231. The monochromated EELS analysis was supported by an Early Career project supported by DOE Office of Science FWP #ERKCZ55–KC040304 and was performed at Oak Ridge National Laboratory's (ORNL) Center for Nanophase Materials Sciences (CNMS), which is a DOE Office of Science User Facility.

REFERENCES

1. Mandal, S.; Roy, D.; Chaudhari, R. V.; Sastry, M., Pt and Pd Nanoparticles Immobilized on Amine-Functionalized Zeolite: Excellent Catalysts for Hydrogenation and Heck Reactions. *Chem. Mater.* **2004**, *16*, 3714-3724.
2. Balanta, A.; Godard, C.; Claver, C., Pd Nanoparticles for C–C Coupling Reactions. *Chem. Soc. Rev.* **2011**, *40*, 4973-4985.
3. Farrauto, R. J.; Heck, R. M., Catalytic Converters: State of the Art and Perspectives. *Catal. Today* **1999**, *51*, 351-360.

4. Choi, S.-I.; Herron, J. A.; Scaranto, J.; Huang, H.; Wang, Y.; Xia, X.; Lv, T.; Park, J.; Peng, H.-C.; Mavrikakis, M.; Xia, Y., A Comprehensive Study of Formic Acid Oxidation on Palladium Nanocrystals with Different Types of Facets and Twin Defects. *ChemCatChem* **2015**, *7*, 2077-2084.
5. Lu, X.; Ahmadi, M.; DiSalvo, F. J.; Abruña, H. D., Enhancing the Electrocatalytic Activity of Pd/M (M = Ni, Mn) Nanoparticles for the Oxygen Reduction Reaction in Alkaline Media through Electrochemical Dealloying. *ACS Catal.* **2020**, *10*, 5891-5898.
6. Zhao, Y.; Tan, X.; Yang, W.; Jia, C.; Chen, X.; Ren, W.; Smith, S. C.; Zhao, C., Surface Reconstruction of Ultrathin Palladium Nanosheets during Electrocatalytic CO_2 Reduction. *Angew. Chem. Int. Ed.* **2020**, *59*, 21493-21498.
7. Herron, J. A.; Scaranto, J.; Ferrin, P.; Li, S.; Mavrikakis, M., Trends in Formic Acid Decomposition on Model Transition Metal Surfaces: A Density Functional Theory Study. *ACS Catal.* **2014**, *4*, 4434-4445.
8. Scaranto, J.; Mavrikakis, M., Density Functional Theory Studies of HCOOH Decomposition on Pd(111). *Surf. Sci.* **2016**, *650*, 111-120.
9. Zhang, R.; Liu, H.; Wang, B.; Ling, L., Insights into the Preference of CO_2 Formation from HCOOH Decomposition on Pd Surface: A Theoretical Study. *J. Phys. Chem. C* **2012**, *116*, 22266-22280.
10. Li, S.; Rangarajan, S.; Scaranto, J.; Mavrikakis, M., On the Structure Sensitivity of and CO Coverage Effects on Formic Acid Decomposition on Pd Surfaces. *Surf. Sci.* **2021**, *709*, 121846.
11. Jiang, K.; Zhang, H.-X.; Zou, S.; Cai, W.-B., Electrocatalysis of Formic Acid on Palladium and Platinum Surfaces: From Fundamental Mechanisms to Fuel Cell Applications. *Phys. Chem. Chem. Phys.* **2014**, *16*, 20360-20376.
12. Hoshi, N.; Kida, K.; Nakamura, M.; Nakada, M.; Osada, K., Structural Effects of Electrochemical Oxidation of Formic Acid on Single Crystal Electrodes of Palladium. *J. Phys. Chem. B* **2006**, *110*, 12480-12484.
13. Rettenmaier, C.; Arán-Ais, R. M.; Timoshenko, J.; Rizo, R.; Jeon, H. S.; Kühl, S.; Chee, S. W.; Bergmann, A.; Roldan Cuenya, B., Enhanced Formic Acid Oxidation over SnO_2-Decorated Pd Nanocubes. *ACS Catal.* **2020**, *10*, 14540-14551.

14. Ye, L.; Mahadi, A. H.; Saengruengrit, C.; Qu, J.; Xu, F.; Fairclough, S. M.; Young, N.; Ho, P.-L.; Shan, J.; Nguyen, L.; Tao, F. F.; Tedsree, K.; Tsang, S. C. E., Ceria Nanocrystals Supporting Pd for Formic Acid Electrocatalytic Oxidation: Prominent Polar Surface Metal Support Interactions. *ACS Catal.* **2019**, *9*, 5171-5177.
15. Shi, Y.; Lyu, Z.; Cao, Z.; Xie, M.; Xia, Y., How to Remove the Capping Agent from Pd Nanocubes without Destructing Their Surface Structure for the Maximization of Catalytic Activity? *Angew. Chem. Int. Ed.* **2020**, *59*, 19129-19135.
16. Liang, Z.; Song, L.; Elnabawy, A. O.; Marinkovic, N.; Mavrikakis, M.; Adzic, R. R., Platinum and Palladium Monolayer Electrocatalysts for Formic Acid Oxidation. *Top. Catal.* **2020**, *63*, 742-749.
17. Shen, T.; Chen, S.; Zeng, R.; Gong, M.; Zhao, T.; Lu, Y.; Liu, X.; Xiao, D.; Yang, Y.; Hu, J.; Wang, D.; Xin, H. L.; Abruña, H. D., Tailoring the Antipoisoning Performance of Pd for Formic Acid Electrooxidation *via* an Ordered PdBi Intermetallic. *ACS Catal.* **2020**, *10*, 9977-9985.
18. Zhang, J.; Chen, M.; Li, H.; Li, Y.; Ye, J.; Cao, Z.; Fang, M.; Kuang, Q.; Zheng, J.; Xie, Z., Stable Palladium Hydride as a Superior Anode Electrocatalyst for Direct Formic Acid Fuel Cells. *Nano Energy* **2018**, *44*, 127-134.
19. Kabiraz, M. K.; Kim, J.; Lee, W.-J.; Ruqia, B.; Kim, H. C.; Lee, S.-U.; Kim, J.-R.; Paek, S.-M.; Hong, J. W.; Choi, S.-I., Ligand Effect of Shape-Controlled *β*-Palladium Hydride Nanocrystals on Liquid-Fuel Oxidation Reactions. *Chem. Mater.* **2019**, *31*, 5663-5673.
20. Sakintuna, B.; Lamari-Darkrim, F.; Hirscher, M., Metal Hydride Materials for Solid Hydrogen Storage: A Review. *Int. J. Hydrog. Energy* **2007**, *32*, 1121-1140.
21. Huang, H.; Bao, S.; Chen, Q.; Yang, Y.; Jiang, Z.; Kuang, Q.; Wu, X.; Xie, Z.; Zheng, L., Novel Hydrogen Storage Properties of Palladium Nanocrystals Activated by a Pentagonal Cyclic Twinned Structure. *Nano Res.* **2015**, *8*, 2698-2705.
22. Zhao, Z.; Huang, X.; Li, M.; Wang, G.; Lee, C.; Zhu, E.; Duan, X.; Huang, Y., Synthesis of Stable Shape-Controlled Catalytically Active *β*-Palladium Hydride. *J. Am. Chem. Soc.* **2015**, *137*, 15672-15675.
23. Lu, Y.; Wang, J.; Peng, Y.; Fisher, A.; Wang, X., Highly Efficient and Durable Pd Hydride Nanocubes Embedded in 2D Amorphous NiB Nanosheets for Oxygen Reduction Reaction. *Adv. Energy Mater.* **2017**, *7*, 1700919.

24. Xu, W.; Fan, G.; Chen, J.; Li, J.; Zhang, L.; Zhu, S.; Su, X.; Cheng, F.; Chen, J., Nanoporous Palladium Hydride for Electrocatalytic N_2 Reduction under Ambient Conditions. *Angew. Chem. Int. Ed.* **2020**, *59*, 3511-3516.
25. Ulvestad, A.; Welland, M. J.; Collins, S. S. E.; Harder, R.; Maxey, E.; Wingert, J.; Singer, A.; Hy, S.; Mulvaney, P.; Zapol, P.; Shpyrko, O. G., Avalanching Strain Dynamics During the Hydriding Phase Transformation in Individual Palladium Nanoparticles. *Nat. Commun.* **2015**, *6*, 10092.
26. Baldi, A.; Narayan, T. C.; Koh, A. L.; Dionne, J. A., In situ Detection of Hydrogen-Induced Phase Transitions in Individual Palladium Nanocrystals. *Nat. Mater.* **2014**, *13*, 1143.
27. Narayan, T. C.; Hayee, F.; Baldi, A.; Leen Koh, A.; Sinclair, R.; Dionne, J. A., Direct Visualization of Hydrogen Absorption Dynamics in Individual Palladium Nanoparticles. *Nat. Commun.* **2017**, *8*, 14020.
28. Johnson, N. J. J.; Lam, B.; MacLeod, B. P.; Sherbo, R. S.; Moreno-Gonzalez, M.; Fork, D. K.; Berlinguette, C. P., Facets and Vertices Regulate Hydrogen Uptake and Release in Palladium Nanocrystals. *Nat. Mater.* **2019**, *18*, 454-458.
29. Lin, B.; Wu, X.; Xie, L.; Kang, Y.; Du, H.; Kang, F.; Li, J.; Gan, L., Atomic Imaging of Subsurface Interstitial Hydrogen and Insights into Surface Reactivity of Palladium Hydrides. *Angew. Chem. Int. Ed.* **2020**, *59*, 20348-20352.
30. Jin, M.; Liu, H.; Zhang, H.; Xie, Z.; Liu, J.; Xia, Y., Synthesis of Pd Nanocrystals Enclosed by {100} Facets and with Sizes <10 nm for Application in CO Oxidation. *Nano Res.* **2011**, *4*, 83-91.
31. Jin, M.; Zhang, H.; Xie, Z.; Xia, Y., Palladium Nanocrystals Enclosed by {100} and {111} Facets in Controlled Proportions and Their Catalytic Activities for Formic Acid Oxidation. *Energy Environ. Sci.* **2012**, *5*, 6352-6357.
32. Zhu, S.; Jiang, B.; Cai, W.-B.; Shao, M., Direct Observation on Reaction Intermediates and the Role of Bicarbonate Anions in CO_2 Electrochemical Reduction Reaction on Cu Surfaces. *J. Am. Chem. Soc.* **2017**, *139*, 15664-15667.
33. Kresse, G.; Furthmüller, J., Efficiency of *ab-initio* Total Energy Calculations for Metals and Semiconductors Using a Plane-Wave Basis Set. *Comput. Mater. Sci.* **1996**, *6*, 15-50.

34. Kresse, G.; Furthmüller, J., Efficient Iterative Schemes for *ab initio* Total-Energy Calculations Using a Plane-Wave Basis Set. *Phys. Rev. B* **1996**, *54*, 11169-11186.
35. Hammer, B.; Hansen, L. B.; Nørskov, J. K., Improved Adsorption Energetics within Density-Functional Theory Using Revised Perdew-Burke-Ernzerhof functionals. *Phys. Rev. B* **1999**, *59*, 7413-7421.
36. Grimme, S.; Ehrlich, S.; Goerigk, L., Effect of the Damping Function in Dispersion Corrected Density Functional Theory. *J. Comput. Chem.* **2011**, *32*, 1456-1465.
37. Haynes, W. M., *CRC Handbook of Chemistry and Physics*. CRC Press: 2016.
38. Zimmerman, J. A.; Hoyt, J. J.; Leonard, F. L.; Griffin, J. D.; Zhou, X. W. *Development of an Inter-Atomic Potential for the Pd-H Binary System*, SAND2007-5976; CA, 2007.
39. Ciufo, R. A.; Henkelman, G., Embedded Atom Method Potential for Hydrogen on Palladium Surfaces. *J. Mol. Model.* **2020**, *26*, 336.
40. Chang, Q.; Kim, J.; Lee, J. H.; Kattel, S.; Chen, J. G.; Choi, S.-I.; Chen, Z., Boosting Activity and Selectivity of CO_2 Electroreduction by Pre-Hydridizing Pd Nanocubes. *Small* **2020**, *16*, 2005305.
41. Manchester, F. D.; San-Martin, A.; Pitre, J. M., The H-Pd (Hydrogen-Palladium) System. *J. Phase Equilib.* **1994**, *15*, 62-83.
42. Worsham, J. E.; Wilkinson, M. K.; Shull, C. G., Neutron-Diffraction Observations on the Palladium-Hydrogen and Palladium-Deuterium Systems. *J. Phys. Chem. Solids* **1957**, *3*, 303-310.
43. Guo, R.; Zhang, K.; Liu, Y.; He, Y.; Wu, C.; Jin, M., Hydrothermal Synthesis of Palladium Nitrides as Robust Multifunctional Electrocatalysts for Fuel Cells. *J. Mater. Chem. A* **2021**, *9*, 6196-6204.
44. Liu, D. R.; Brown, L. M., Characterization of Palladium Hydride Films by Electron Energy Loss Spectroscopy and Electron Diffraction. *Acta Metall.* **1988**, *36*, 2597-2604.
45. Hirabayashi, M.; Asano, H., Metal Hydrides, Ed. by G. Bambakidis. Plenum Press, NY: 1981, p.230.
46. Albers, P.; Poniatowski, M.; Parker, S. F.; Ross, D. K., Inelastic Neutron Scattering Study on Different Grades of Palladium of Varying Pretreatment. *J. Phys. Condens. Matter* **2000**, *12*, 4451-4463.

47. Parker, S. F.; Walker, H. C.; Callear, S. K.; Grünewald, E.; Petzold, T.; Wolf, D.; Möbus, K.; Adam, J.; Wieland, S. D.; Jiménez-Ruiz, M.; Albers, P. W., The Effect of Particle Size, Morphology and Support on the Formation of Palladium Hydride in Commercial Catalysts. *Chem. Sci.* **2019**, *10*, 480-489.
48. Venkatraman, K.; March, K.; Rez, P.; Crozier, P. A., Aloof-beam Vibrational Electron Energy-Loss Spectroscopy of Adsorbate/Metal Particle Systems. *Microsc. Microanal.* **2018**, *24*, 460-461.
49. Riesterer, T., Electronic Structure and Bonding in Metal Hydrides, Studied with Photoelectron Spectroscopy. *Z. Phys., B Condens. Matter.* **1987**, *66*, 441-458.
50. Houari, A.; Matar, S. F.; Eyert, V., Electronic Structure and Crystal Phase Stability of Palladium Hydrides. *J. Appl. Phys.* **2014**, *116*, 173706.
51. Chan, C. T.; Louie, S. G., Self-Consistent Pseudopotential Calculation of the Electronic Structure of PdH and Pd_4H. *Phys. Rev. B* **1983**, *27*, 3325-3337.
52. Bennett, P. A.; Fuggle, J. C., Electronic Structure and Surface Kinetics of Palladium Hydride Studied with X-Ray Photoelectron Spectroscopy and Electron-Energy-Loss Spectroscopy. *Phys. Rev. B* **1982**, *26*, 6030-6039.
53. Zheng, M.; Cheng, R.; Chen, X.; Li, N.; Li, L.; Wang, X.; Zhang, T., A Novel Approach for CO-Free H_2 Production *via* Catalytic Decomposition of Hydrazine. *Int. J. Hydrog. Energy* **2005**, *30*, 1081-1089.
54. Borodko, Y.; Lee, H. S.; Joo, S. H.; Zhang, Y.; Somorjai, G., Spectroscopic Study of the Thermal Degradation of PVP-Capped Rh and Pt Nanoparticles in H_2 and O_2 Environments. *J. Phys. Chem. C* **2010**, *114*, 1117-1126.
55. Rao, V.; Latha, P.; Ashokan, P. V.; Shridhar, M. H., Thermal Degradation of Poly(N-vinylpyrrolidone)–Poly(vinyl alcohol) Blends. *Polym. J. (Tokyo, Jpn.)* **1999**, *31*, 887-889.
56. Oates, W. A.; Flanagan, T. B., The Reaction of Hydrogen Atoms with Palladium and its Alloys. *Can. J. Chem.* **1975**, *53*, 694-701.
57. Simpson, D. *Safety and handling of hydrazine*; ADP005339; OLIN CORP CHESHIRE CT OLIN RESEARCH CENTER: 1986.
58. Zalineeva, A.; Baranton, S.; Coutanceau, C.; Jerkiewicz, G., Electrochemical Behavior of Unsupported Shaped Palladium Nanoparticles. *Langmuir* **2015**, *31*, 1605-1609.

59. Moseley, P.; Curtin, W. A., Computational Design of Strain in Core–Shell Nanoparticles for Optimizing Catalytic Activity. *Nano Lett.* **2015**, *15*, 4089-4095.
60. Schimmenti, R.; Mavrikakis, M., HCOOH Decomposition on Sub-Nanometer Pd_6 Cluster Catalysts: The Effect of Defective Boron Nitride Supports Through First Principles. *Appl. Catal. B* **2021**, *280*, 119392.
61. Schimmenti, R.; Cortese, R.; Duca, D.; Mavrikakis, M., Boron Nitride-Supported Sub-Nanometer Pd_6 Clusters for Formic Acid Decomposition: A DFT Study. *ChemCatChem* **2017**, *9*, 1610-1620.
62. Bradshaw, A. M.; Hoffmann, F. M., The Chemisorption of Carbon Monoxide on Palladium Single Crystal Surfaces: IR Spectroscopic Evidence for Localised Site Adsorption. *Surf. Sci.* **1978**, *72*, 513-535.

TOC graphic